Constant Motion, Acceleration, Vibration, and Rotation of Objects in SAR Data

Maurice Rüegg, Erich Meier and Daniel Nüesch

Remote Sensing Laboratories, University of Zürich, CH-8057 Zürich, Switzerland

ABSTRACT

Synthetic aperture radar (SAR) provides high resolution images of static ground scenes, but processing of data containing moving objects results in varying phase and amplitude effects. The work at hand illustrates via theoretical considerations and concrete simulations what happens to SAR imagery when parts of a scene are not static. We differentiate between four types of motion. Objects moving with a constant velocity cause position errors in azimuth as well as target defocusing and smearing in azimuth and range. Accelerating objects are responsible for even stronger shift and defocusing effects since the position errors are now a function of time. Closely related are vibrations of an object. They may be interpreted as a regular and continuous de- and acceleration whose range component results in so-called paired echoes on each side of an object in azimuth. Finally, rotation as an extreme example of constant radial acceleration may disturb a SAR image over a wide area. Through a thorough motion analysis, we developed a flexible SAR raw data simulator. Our simulations of point scatterers in raw data are based on the radar radiation pattern as a function of the system carrier frequency and the relative positions between the radar and each scatterer. All four types of movement described above may be expressed as varying relative positions and Doppler frequency shifts due to instantaneous phase variations. The standard SAR processing steps of range and azimuth compression for the simulated data provide impressive results for freely adaptable system parameters of the movement and of the SAR system.

Keywords: Synthetic Aperture Radar, Moving Target Indication, SAR Raw Data Simulations

1. INTRODUCTION

SAR raw data simulations have been a topic of interest for many years,[1–3] seeing an ever-growing level of complexity, detail, and consideration of real-world parameters. On the other hand, constraining complexity and laying emphasis on a single phenomenon is a great strength of simulations as opposed to real, meaning experimental SAR data. This is especially true when looking at moving target indication (MTI). The fundamental theory on SAR MTI is long known.[4] Because experimental MTI data may be very complex (non-regular target accelerations, non-linear target tracks, strong background clutter, etc.), simulations help identify and overcome some common obstacles by providing raw SAR data sets with clearly defined movements.[5]

It is not the aim of our work to present MTI algorithms. For this, we would like to refer to References 6–8. Instead, we look into some mathematically well describable object movements and their effects on SAR images. To be able to do this, we first define a simple two-dimensional radar geometry and a SAR system model for static point targets used as a basis for simulations in Section 2. We extend this model first to include constant motion in Section 3 and subsequently constant acceleration in Section 4. With some meaningful examples of visual effects we discuss our theoretical models. Section 5 analyzes vibrating point targets in SAR. There have been experimental observations on vibration before,[9–12] but not with ideal data from a simulator where effects are well defined and clearly visible. Before concluding our analysis in Section 7, we discuss target rotation in Section 6 and some of its very interesting implications. For all simulations, our emphasis lies on a theoretical model that incorporates all relevant effects of point target motion patterns and on the visual effects these patterns evoke in a focused SAR image.

2. SAR STATIC SCENES

The following SAR geometry and system model for static point targets are based on the well described theory from chapter 6.1 of Reference 1. Because we use them as a foundation to all subsequent considerations, they are explained in detail in Section 2.1 and 2.2.

SAR Image Analysis, Modeling, and Techniques VII, edited by Francesco Posa,
Proc. of SPIE Vol. 5980, 598005, (2005) · 0277-786X/05/$15 · doi: 10.1117/12.626529

2.1. Geometry

We use a purely two-dimensional sensor flight geometry, with the x-coordinate pointing right in the radar look direction (range) and the y-coordinate pointing down in the flight direction (azimuth). We assume an airborne stripmap SAR system on a linear flight track and neglect spaceborne data effects of earth rotation and orbit curvature. All image dimensions are given by the target area of interest, the SAR antenna radiation pattern, and the resulting recorded scene as described in Figure 1. The antenna radiation pattern defines the 3 dB beam width of the SAR. We model the signal inside this 3dB beam width through its transfer function, given as

$$H(\omega, x, y-u) = A(\omega, x, y-u) \cdot \exp\left(-2j\frac{\omega}{c}\sqrt{x^2+(y-u)^2}\right). \tag{1}$$

Obviously, the phase as well as the amplitude $A(\omega, x, y-u)$ in (1) depend on the signal frequency ω and the relative position between a scatterer at (x, y) and the SAR sensor at $(0, u)$. c is the speed of light.

The area of validity (3 dB beam width) of the antenna is strongly dependent on the type of antenna used (planar array or curved antenna) and its specifications. For our model, we make do with a simple pattern defined via the 3 dB half-beam width B with

$$B(x) = x \cdot \tan(\phi_d). \tag{2}$$

This implies the knowledge of the size of the antenna aperture angle ϕ_d which is approximated in Reference 1 via the carrier wavelength λ_c and the physical antenna diameter in azimuth D_y as

$$\phi_d = \text{asin}(\frac{\lambda_c}{D_y}). \tag{3}$$

Let us now define the target area of interest in azimuth by

$$y \in [-Y_0, Y_0]. \tag{4}$$

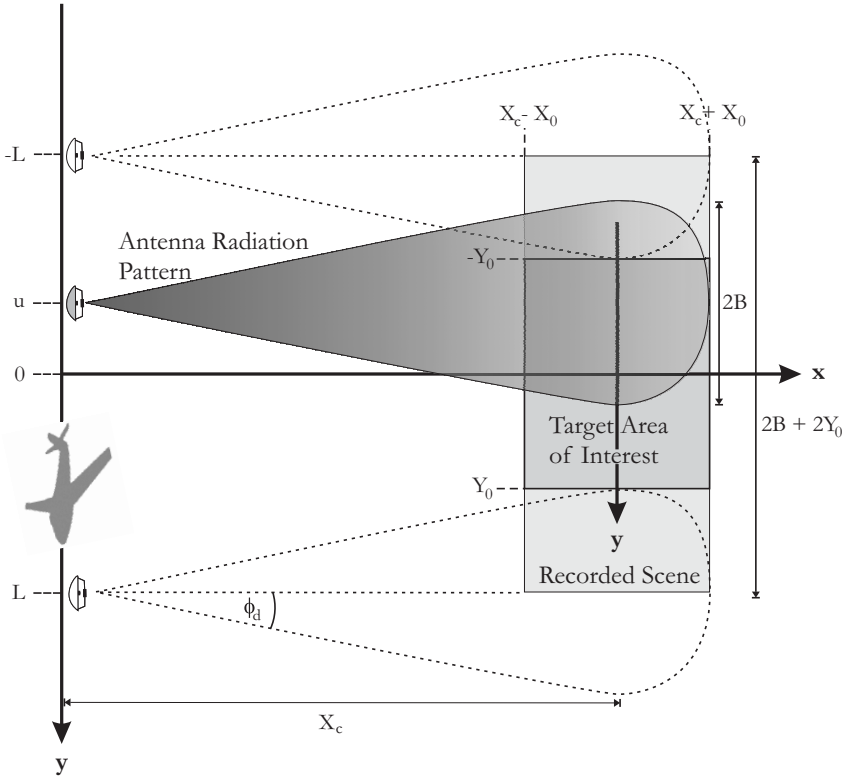

Figure 1. Imaging geometry of stripmap SAR. Flight direction or azimuth is denoted by y and radar looking direction or range by x.

In order to receive data from the full synthetic aperture of all targets inside the area of interest, we extend the azimuth recorded scene (see Figure 1) and define the radar position u to be valid inside

$$u \in [-L, L] \tag{5}$$

where

$$L = B + Y_0. \tag{6}$$

In range, we define the target area of interest simply through its extent X_0 on each side of the scene center X_c. Ergo

$$x \in [X_c - X_0, X_c + X_0]. \tag{7}$$

2.2. System Model

After having defined a target geometry, we would like to analyze and simulate raw SAR data. Raw data have the advantage over single look complex focused SAR images in that we remain more flexible when evaluating focusing techniques and MTI algorithms as well as that we have an additional level of information, namely the unprocessed amplitude and phase of targets.

We start by defining the emitted radar signal. Most current SAR systems use a frequency modulated chirp signal. Thus, we define such a chirp p as a function of the fast time (time in range) for our system model as

$$p(t) = e^{j(\beta t + \alpha t^2)}. \tag{8}$$

α is known as the chirp rate. (8) implies that we use a carrier frequency

$$\omega_c = \beta + \alpha\tau_p \tag{9}$$

where τ_p is the pulse duration and that our bandwidth is set as

$$\pm\omega_0 = \pm\alpha\tau_p. \tag{10}$$

The Fourier transform of (8) is defined as

$$P(\omega) = \int_{-\infty}^{\infty} p(t) \cdot e^{-j\omega t} dt. \tag{11}$$

Together with the transfer function from (1) we receive an echo at the antenna position u from a point target n at location $\mathbf{Q}_n = (x_n, y_n)$ defined by

$$\begin{aligned} S(\omega, u) &= P(\omega) \cdot \sum_n H_n(\omega, x_n, y_n - u) \\ &= P(\omega) \cdot \sum_n a_n(\omega, x_n, y_n - u) \cdot A_n \exp\left(-2j\frac{\omega}{c}\sqrt{x_n^2 + (y_n - u)^2}\right). \end{aligned} \tag{12}$$

While A_n is the constant omni-directional target reflectivity, a_n is the return echo amplitude depending on position and frequency. More exactly, we use the target aspect angle

$$\theta_n(u) = \text{atan}\left(\frac{y_n - u}{x_n}\right) \tag{13}$$

to define the signal amplitude of the nth target as a raised cosine

$$a_n(\omega, x_n, y_n - u) = \frac{1}{2} + \frac{1}{2} cos\left(\frac{\pi\theta_n(u)}{\phi_d(\omega)}\right). \tag{14}$$

We note that the antenna aperture angle is given depending on ω which may be important for wideband systems. Instead of (3) we set $\phi_d(\omega) = \text{asin}(\frac{2\pi c}{\omega D_y})$. With $u \in [y_n - B_n, y_n + B_n]$ and $B_n = x_n \tan(\phi_d)$ we receive a target amplitude different from zero within the synthetic aperture of the radar.

Finally, we shift our received raw SAR signal to the baseband with

$$s_B(t, u) = s(t, u) \cdot e^{-j\omega_c t}. \tag{15}$$

2.3. Processing and Simulations

Once we have complex-valued raw SAR data in the baseband, we may apply any of numerous SAR focusing approaches such as the Range-Doppler, $\omega - k$, or Chirp Scaling algorithms.[13,14] We use the Extended Chirp Scaling algorithm[15] for all focused SAR data presented in the following because of its computational efficiency.

For demonstration purposes and without loss of generality, we define an imaginary airborne X-band SAR system of $f_c = 10$ GHz carrier frequency, a system bandwidth of $2\omega_0 = 200$ MHz and pulse duration of $\tau_p = 0.5\ \mu s$, a pulse repetition frequency (PRF) of 2 kHz, and a SAR sensor speed in azimuth of $v_s = 100$ m/s. We choose a planar array antenna with $D_y = 1$ m. If not indicated otherwise, we use these same parameters for all simulations presented in this work. The relatively high PRF is chosen to exclude special MTI effects to be discussed in Section 3.2. The decision to use the described X-band system is based on the fact that some prominent experiments focus on this band[8,16] and that processing of such data is relatively straightforward.

Furthermore, we define a target area 5000 m distant from the sensor and place five point targets: one center target and four surrounding targets forming a perfect square of edge length 100 m. There is neither clutter nor receiver noise. The resulting amplitude and phase images of the raw as well as the range compressed and the fully focused images are shown in Figure 2. The image resolution in Figure 2 and all subsequent SAR images is 0.75×0.75 m^2.

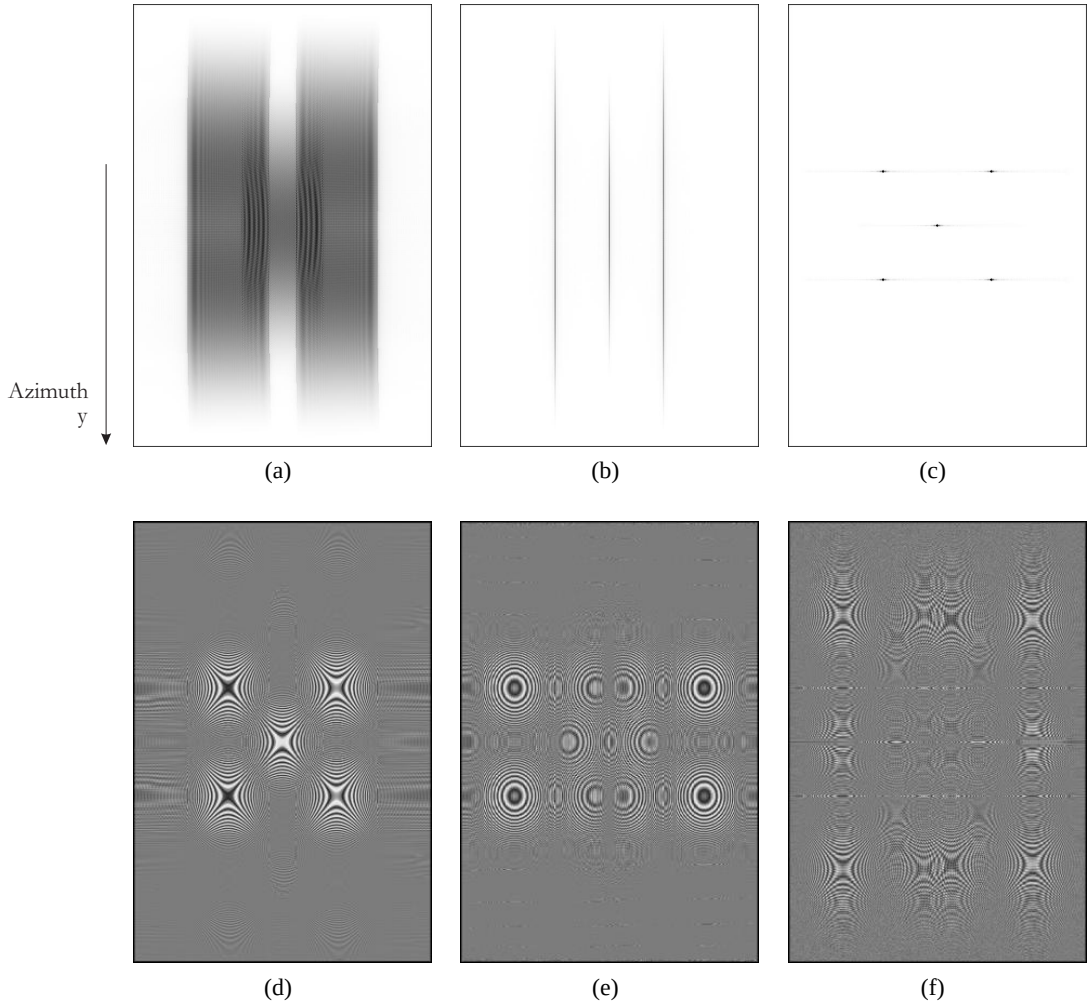

Figure 2. SAR scene of five static point targets forming a square with 100 m edge length as observed by a 10 GHz system with 200 MHz bandwidth and 2 kHz PRF. Top row: amplitude images of (a) raw, (b) range compressed and (c) fully focused data. Bottom row: phase images of (d) raw, (e) range compressed and (f) fully focused data.

The superposition of the five targets in Figure 2 is nicely visible in the raw and range compressed data amplitude, while at the same time, it makes the images hard to read. Only the fully focused amplitude image allows for a clear identification of each individual target. Interpreting the phase is easier for the raw image and becoming very demanding for the range compressed and fully focused data.

3. CONSTANT MOTION

3.1. Extended System Model

A first extension to our system model defined in Section 2.2 is the addition of constant motion to point targets. Hence, a target n is defined through its position $\mathbf{Q}_n(0) = (x_n, y_n)$ at azimuth time zero (defined by u/v_s at sensor position $u = 0$) and its velocity vector (v_{x_n}, v_{y_n}). At sensor position u, we get a target position

$$\mathbf{Q}_n(u) = \begin{pmatrix} x_n + v_{x_n} u/v_s \\ y_n - u + v_{y_n} u/v_s \end{pmatrix}. \tag{16}$$

When inserting (16) into (12) we get an echo signal at the antenna from all targets n

$$S(\omega, u) = P(\omega) \cdot \sum_n a_n(\omega, x_n, y_n - u) \cdot A_n \exp\left(\frac{-2j\omega}{c} \sqrt{\left(x_n + \frac{uv_{x_n}}{v_s}\right)^2 + \left(y_n - u + \frac{uv_{y_n}}{v_s}\right)^2} \right). \tag{17}$$

Because of the target movement, the target aspect angle $\theta_n(u)$ defined in (13) must be adapted to

$$\theta_n(u) = \text{atan}\left(\frac{y_n - u + \frac{uv_{y_n}}{v_s}}{x_n + \frac{uv_{x_n}}{v_s}} \right) = \text{atan}\left(\frac{v_s(y_n - u) + uv_{y_n}}{v_s x_n + uv_{x_n}} \right). \tag{18}$$

Secondly, a moving target experiences a Doppler shift[4] that is dependent on the radial target velocity $v_{r_n}(u)$:

$$f_{D_n}(u) = -\frac{\omega_c v_{r_n}(u)}{\pi c} \tag{19}$$

with the instantaneous radial target velocity given by

$$v_{r_n}(u) = v_{x_n} \cos(\theta_n(u)) + v_{y_n} \sin(\theta_n(u)). \tag{20}$$

(19) is negative because we define a positive radial velocity to point away from the radar (according to the x-coordinate of the geometry).

Finally, we may combine the operations of baseband conversion and Doppler shift correction for each target n as

$$s_{B_n}(t, u) = s_n(t, u) \cdot e^{-j(\omega_c + 2\pi f_{D_n})t}. \tag{21}$$

3.2. Visual Effects

It is well known that a moving target may be smeared, defocused and displaced in azimuth in a focused SAR image.[4, 6] While the smearing and defocusing are direct effects of a changing target position inside the synthetic aperture, the displacement is due to the Doppler shift of (19). The amount of the shift in azimuth is given as[17]

$$d_n = -\frac{v_{r_n}}{v_s} x_n. \tag{22}$$

In Figure 3, three different constant target movements are shown. We use the same SAR system and geometry parameters as in Section 2.3 with the one difference that our center target is now moving. If the movement is radial as in Figure 3(a), where we set $v_x = 1$ m/s, we get a displacement in y of exactly -50 m according to (22). If the movement is tangential as in Figure 3(b) ($v_y = 3$ m/s), we get a smearing effect but no displacement. Figure 3(c) shows a combination of radial and tangential movement.

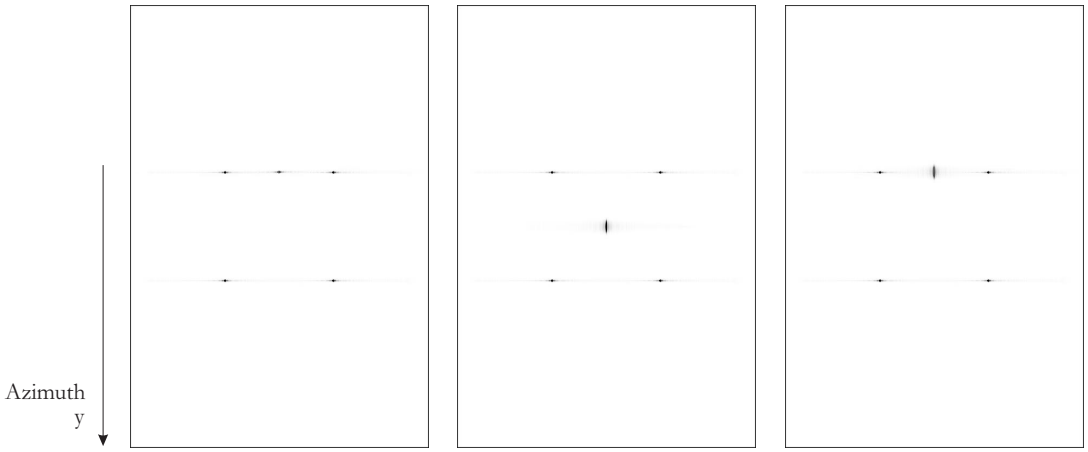

Figure 3. Focused SAR scenes with a moving center target. In (a), the target is moving right with $v_x = 1$ m/s, causing a displacement in azimuth. (b) shows a smeared target moving down with $v_y = 3$ m/s. In (c), the target moves right with 1 m/s and down with 3 m/s.

There are some effects that must be considered when dealing with moving targets in SAR imagery; they may be summarized as Doppler ambiguities and blind speeds,[18] and they appear because of a limited PRF. They are illustrated in Figure 4. When the Doppler shift of a target due to its radial velocity approaches half the PRF because of a large velocity or small PRF, a target is displaced in negative as well as positive direction (Figure 4(b), PRF reduced to 133.3 Hz). If a positive radial target velocity is above half the PRF the movement becomes ambiguous in the SAR (it might just as well be a negative velocity) and when it reaches the PRF, its Doppler shift is folded inside the PRF as 0 Hz and we do not get a displacement at all (Figure 4(c), PRF reduced to 66.7 Hz). Only smearing might then point to a moving target.

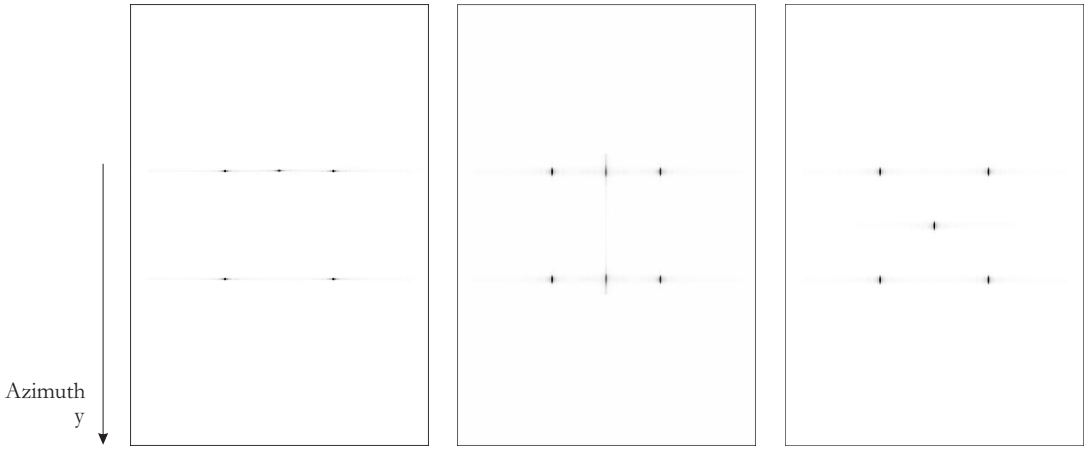

Figure 4. SAR Scenes with a moving center target (to the right at 1 m/s) at different PRFs. (a) is the reference image from Figure 3 where the PRF is 2000 Hz. (b) shows the same scene recorded at a PRF of 133.3 Hz and (c) at 66.7 Hz. (Due to the decreased PRF, the image resolution is also decreased, which is clearly visible for the static reference targets.)

4. ACCELERATION

4.1. Extended System Model

When considering acceleration we simply add an acceleration vector (a_{x_n}, a_{y_n}) for each target to our extended system model of Section 3.1 and get an instantaneous target position

$$\mathbf{Q}_n(u) = \begin{pmatrix} x_n + \frac{u}{v_s}\left(v_{x_n} + \frac{u}{2v_s}a_{x_n}\right) \\ y_n - u + \frac{u}{v_s}\left(v_{y_n} + \frac{u}{2v_s}a_{y_n}\right) \end{pmatrix}. \tag{23}$$

We note that this model even allows for velocity inversion of direction since $u \in [-L, L]$. From (12) and (23) we receive the echo signal at the antenna for accelerating targets n

$$\begin{aligned} S(\omega, u) &= P(\omega) \cdot \sum_n a_n(\omega, x_n, y_n - u) \cdot A_n \cdot \\ &\exp\left(\frac{-2j\omega}{c}\sqrt{\left(x_n + \frac{u}{v_s}\left(v_{x_n} + \frac{u}{2v_s}a_{x_n}\right)\right)^2 + \left(y_n - u + \frac{u}{v_s}\left(v_{y_n} + \frac{u}{2v_s}a_{y_n}\right)\right)^2}\right) \end{aligned} \tag{24}$$

and the target aspect angle is given as

$$\theta_n(u) = \text{atan}\left(\frac{y_n - u + \frac{u}{v_s}\left(v_{y_n} + \frac{u}{2v_s}a_{y_n}\right)}{x_n + \frac{u}{v_s}\left(v_{x_n} + \frac{u}{2v_s}a_{x_n}\right)}\right). \tag{25}$$

As in Section 3.1, we must consider the Doppler shift of (19), dependent on the radial target velocity. However, this time we have an instantaneous radial velocity that depends additionally on the acceleration of a target

$$v_{r_n}(u) = \left(v_{x_n} + \frac{u}{v_s}a_{x_n}\right)\cos(\theta_n(u)) + \left(v_{y_n} + \frac{u}{v_s}a_{y_n}\right)\sin(\theta_n(u)). \tag{26}$$

4.2. Visual Effects

Figure 5 shows the main effects to be expected from our system model of accelerating targets. In (a), we simulate a target accelerating with 0.5 m/s^2 in range and an instantaneous velocity of 1 m/s at $u = 0$. (b) shows the situation for an azimuth acceleration of 0.5 m/s^2 and an instantaneous velocity at $u = 0$ of 3 m/s. (c) combines the two movements. Because of a non-constant velocity in range, the moving target in (a) gets displaced over a wide range in azimuth, looking like a smeared target. (b) looks very similar to Figure 3(b)—where we had a constant azimuth movement—because the absolut target drift tangential to the radar is almost identical in both situations.

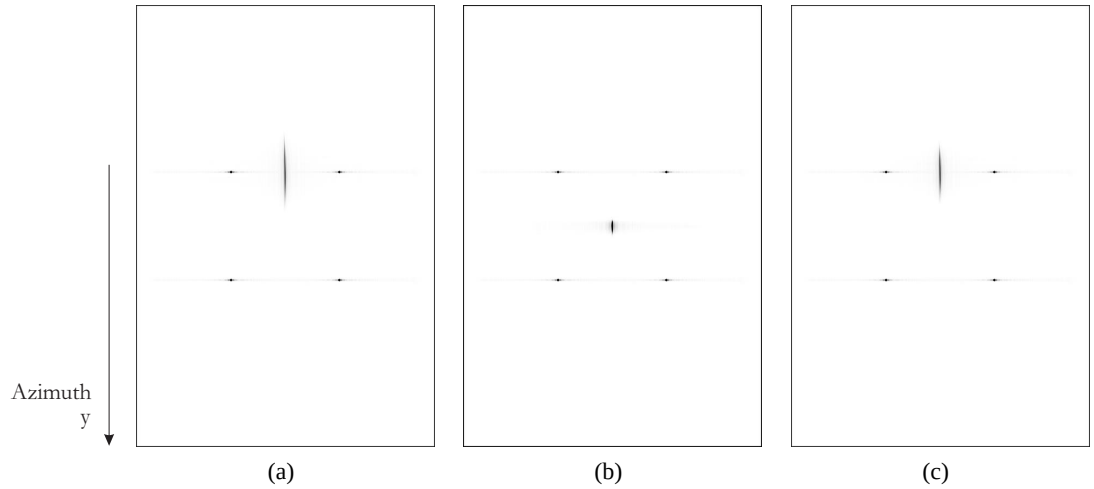

Figure 5. SAR Scenes with an accelerating center target. In (a), the target is accelerating towards the right from about 0.5 to 1.5 m/s. (b) shows a target accelerating downwards from about 2.5 to 3.5 m/s. The combined acceleration of (a) and (b) is shown in (c).

5. VIBRATION

Vibrations are a very interesting movement in SAR imagery. They might originate from a wide range of objects: from a standing vehicle with its motor running to large earth surface areas shaking during an earthquake. As we will see, vibrations cause a phase modulation of the received SAR signals.

5.1. Extended System Model

For our vibrations system model, we use once more our standard model of Section 2.2. We assume effects to be dependent on azimuth time u/v_s and only consider vibrations in range but non in azimuth because vibrations in azimuth would only result in marginal smearing effects of objects. We define a point target n through its vibration in range

$$V_n(u) = A_{V_n} \cos\left(\omega_{V_n} \frac{u}{v_s}\right) \tag{27}$$

with vibration amplitude A_{V_n} and frequency ω_{V_n}, and we get an instantaneous position

$$\mathbf{Q}_n(u) \approx \begin{pmatrix} x_n + V_n(u) \\ y_n \end{pmatrix}. \tag{28}$$

The approximation is valid if we assume a large sensor to target distance and a small antenna aperture ($x_n^2 + (y_n - u)^2 \approx x_n^2$).[12] This enables us to use our standard model defined in Section 2.2. The only additional consideration must be the Doppler shift effects because we may derive the fluctuating target velocity as

$$v_{x_n}(u) = \frac{dV_n}{du} = -A_{V_n} \frac{\omega_{V_n}}{v_s} \sin\left(\omega_{V_n} \frac{u}{v_s}\right). \tag{29}$$

To calculate the target Doppler shift due to the vibration we use once more (20), (19), and (21). Equivalently, we could use the change of phase due to the vibration to get $\Delta\varphi_n(u) = A_{V_n} 4\pi/\lambda_c \cos(\omega_{V_n} u/v_s)$ and a Doppler shift of $f_{D_n}(u) = \frac{1}{2\pi}\frac{\Delta\varphi_n}{du}$. We see that a vibrating target in SAR causes a phase modulation in the received signal phases φ, defined as

$$\varphi(u) = \omega_d + A_{V_n} \frac{4\pi}{\lambda_c} \cos\left(\omega_{V_n} \frac{u}{v_s}\right) \tag{30}$$

where ω_d is the phase history of a static object.

5.2. Visual Effects

The phase modulation causes an effect in SAR images that is known as paired echoes.[9] As the name suggests, we get ghost targets above and below a vibrating target due to the Doppler shifts. In chapter 7.5.2 of Reference 9 the intensity I of a paired echo p is given to be proportional to the vibration amplitude as

$$I_{n,p} \propto \frac{2\pi A_{V_n}}{\lambda_c}. \tag{31}$$

The displacement of paired echo p—assuming that it is still visible when considering (31)—is determined by

$$d_{n,p} = \mp \frac{n\lambda_c \omega_{V_n}}{4\pi} \cdot \frac{1}{v_s} x_n \tag{32}$$

which is directly related to (22).

In Figure 6 we see three examples of vibrating point targets. In (a), we define a target with vibration amplitude $A_{V_n} = 1$ mm and frequency $f_{V_n} = 50$ Hz that generates a single visible paired echo. If we increase the amplitude to 2 mm as in (b), we get a second visible paired echo. In (c), the amplitude is again 1 mm but the frequency is halved to 25 Hz. This halves the displacement distance of the single visible paired echo as compared to (a).

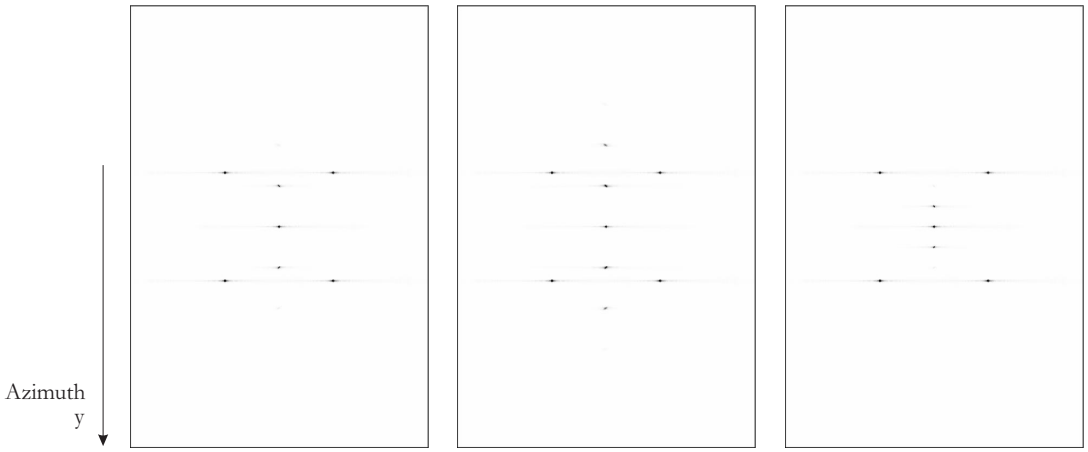

Figure 6. SAR Scenes with a vibrating center target. In (a) and (c), the vibration amplitude is 1 mm, in (b) it is doubled to 2 mm. The vibration frequency for (a) and (b) is 50 Hz and 25 Hz for (c).

6. ROTATION

Rotating objects in SAR images may be rare but are definitely interesting. Examples may be ground based surveillance radar antennas or helicopter rotors. They have very different backscattering but common movement characteristics, closely related to vibrations as we will see in the following definitions.

6.1. Extended System Model

A rotation of a point target and thus an object with radius zero is not defined. Thus we will here develop a model for an extended object consisting of multiple point targets moving in a circle around a common center as shown in Figure 7. All point targets m of a rotating object n share a common rotational frequency ω_{R_n} but have individual radii $r_{m,n}$ from the center (x_n, y_n) of the object. We define the movement of such a point target as

$$\mathbf{Q}_{m,n}(u) = \begin{pmatrix} x_n + r_{m,n} \cos\left(\omega_{R_n} \frac{u}{v_s}\right) \\ y_n + r_{m,n} \sin\left(\omega_{R_n} \frac{u}{v_s}\right) \end{pmatrix}. \tag{33}$$

These positions may easily be incorporated into our standard model for the received echoes at the antenna of (12). Depending on the method we either calculate the instantaneous radial velocity and the Doppler shift according to (19) or we define the phase change $\Delta\varphi_{m,n}(u)$ of m as for vibrations. To use the instantaneous velocity is the direct approach; thus we need the velocity vector given by

$$\frac{d\mathbf{Q}_{m,n}}{du} = \begin{pmatrix} -r_{m,n} \frac{\omega_{R_n}}{v_s} \sin\left(\omega_{R_n} \frac{u}{v_s}\right) \\ r_{m,n} \frac{\omega_{R_n}}{v_s} \cos\left(\omega_{R_n} \frac{u}{v_s}\right) \end{pmatrix}. \tag{34}$$

With (20) and (19), we may then add a Doppler shift into (21).

An important aspect of rotating objects is their change of reflectivity during rotation. If we assume a ground based planar radar antenna as our rotating object, it is clear that the antenna broadside will have a much higher reflectivity than its side profile. Thus, we redefine our so far constant and omni-directional reflectivity A_n to make up for this rotational signal amplitude change by defining for all m of the rotating object n the variable reflectivity

$$A_{m,n}(u) = \frac{A_n}{2m} \left(1 + \left|\sin\left(\omega_{R_n} \frac{u}{v_s}\right)\right|\right). \tag{35}$$

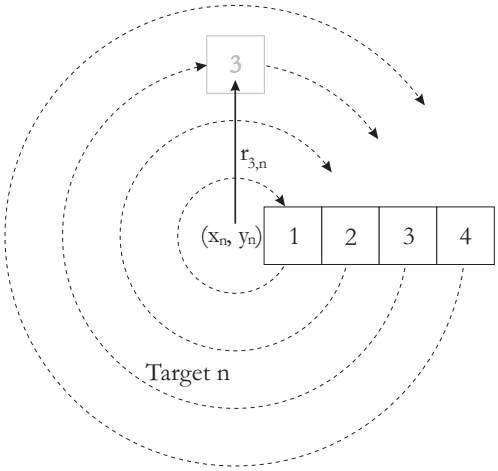

Figure 7. In the rotational system model, an extended rotating object n consists of m point targets moving in a circle around a common center (x_n, y_n) at different radii $r_{n,m}$ and equal frequency ω_{R_n}.

6.2. Visual Effects

Because a rotation implies a constantly changing velocity at every point of an object, we get many and large displacement effects for rotating targets. In Figure 8, three focused example SAR images are shown. The center object has a radius of 0.75 m in (a) and (b)—equal to the image resolution: our object is made up of two point targets circling each other—while in (c), the radius is 1.5 m. In (a) and (c) the rotational frequency is 1 Hz and in (b) 0.5 Hz. Important is the fact that we reduced the PRF compared to all previous simulations by a factor of 10 to 200 Hz. This reduces displacement effects from 3000 to 300 m.

It is clear that the rotational change of the object reflectivity and the PRF also has an influence on what and how many visible displaced positions we get. In Figure 9(a) we show the same situation as in Figure 8(a), however, this time with a constant omnidirectional reflectivity A_n instead of $A_{m,n}(u)$. As expected, the target becomes slightly more distinct.

Considering the PRF, there is the extreme case where the PRF is equal to the frequency of rotation, and we only get a single displaced position for every resolution cell. The higher the difference between the PRF and the frequency of rotation, the more our target will become a smeared image as shown in Figure 9(b) where we used a frequency of rotation

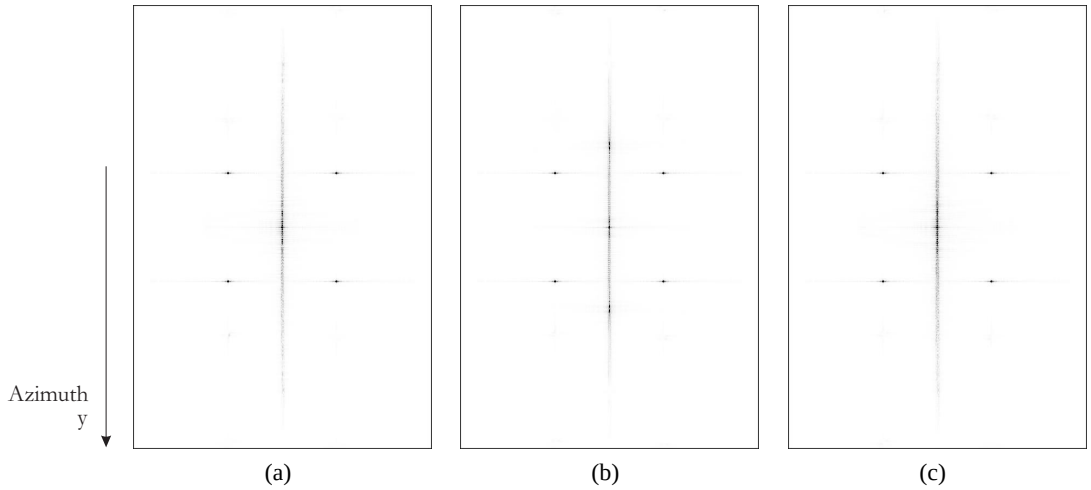

Figure 8. SAR Scenes with a rotating center target. In (a) and (c) the rotation frequency is 1 Hz, in (b) 0.5 Hz. The target radius is 0.75 m for (a) and (b) and 1.5 m for (c). We note that the PRF has been reduced to 200 Hz for these simulations.

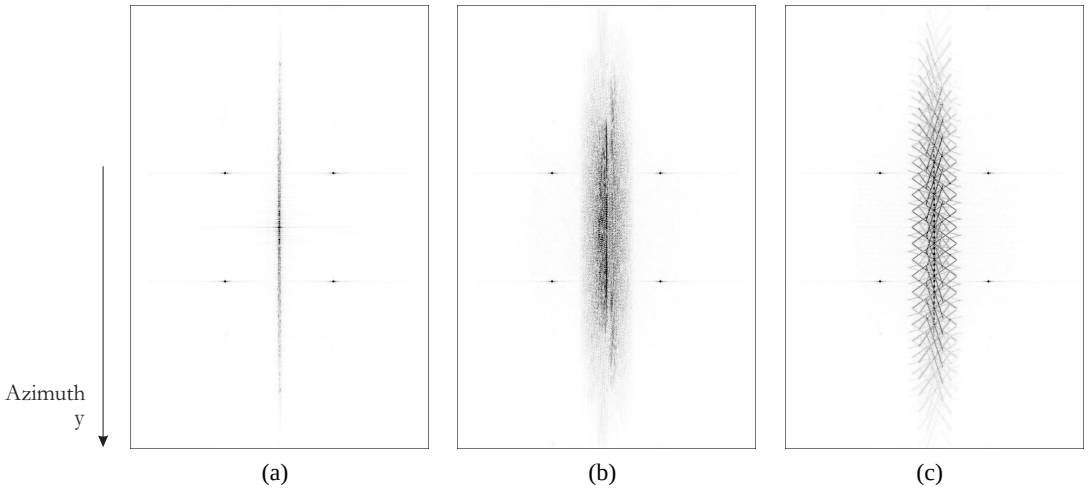

Figure 9. SAR Scenes with a rotating center target. (a) is equal to Figure 8(a) but with a constant omni-directional target reflectivity instead of the one given in (35). (b) and (c) show sampling considerations (PRF = 200 Hz) for large targets (radius 25 m): rotation frequency in (b) is 0.1 Hz and in (c) 10 Hz.

of 0.1 Hz and a very large target radius 25 m and Figure 9(c) where the frequency of rotation is increased to 10 Hz and the SAR pattern of the rotation becomes very regular because of sampling limitations.

7. CONCLUSIONS

A general system model for SAR simulation of static point targets was extended to consider and mathematically define constant motion, acceleration and vibration of point targets as well as extended rotating objects. Results showed some important effects of moving targets. One of the strengths of the presented system model is its flexibility. We defined and simulated movements in SAR raw data and thus reproduced the physical conditions that would be difficult to simulate in focused images.

In defining such a flexible system model and showing SAR image effects of not only constantly moving objects, we covered an important aspect of MTI that is generally neglected in the literature. Acceleration and vibration of targets are not often if at all discussed and described. Even more important, there has not yet been—to the best of our knowledge—any well described theoretical or practical analysis of rotating objects in the open literature.

Our simulations were done using an imaginary but close-to-reality X-band SAR sensor configuration. The presented system model does not include any restrictions towards a specific sensor configuration but works for many specifications. The only approximation is the determination of the antenna beam pattern. It may easily be replaced with an antenna-specific model. For constant motion, the effects of displacement and the extent of smearing could be analyzed. A flexible variation of system parameters illustrated in detail the problems of Doppler ambiguity and blind speeds for small PRFs, high target velocity or both.

The step from modeling constant motion to acceleration in SAR is a small one. The implications of accelerations are difficult to observe in experimental SAR data. Our simulations make it possible to accurately examine such non-constant motions. With vibration and rotation, we analyzed two further motion patterns that may well influence a SAR scene. Being aware of the possibly large implications of a rotating object is important for the interpretation of images. Similarly, the vibration phenomenon of paired echoes not only increases the understanding of SAR processing, but lets one think about possible exploitations for vibration detection techniques.

We restrained ourselves to well defined movements, meaning linear or circular velocities and accelerations. Phase histories of such movements are mathematically representable and thus suitable for simulations. Therefore, they provide a powerful tool to plan moving target experiments for any conceivable SAR sensor configuration and image geometry for many target movement patterns. This is important because we are fully aware that working with simulated data has its downside. Real data will include speckle noise, antenna and atmospheric attenuation, as well as non-ideal targets and

changing target reflectivity effects. How far such effects interfere with our theoretical system model is difficult to predict. We are thus currently in the process of planning a real world experiment scheduled for later this year.

REFERENCES

1. M. Soumekh, *Synthetic Aperture Radar Signal Processing*, John Wiley & Sons, Inc., New York, 1999.
2. J. C. Holtzman, V. S. Frost, J. L. Abbott, and V. H. Kaupp, "Radar Image Simulation," *IEEE Transactions on Geoscience and Remote Sensing* **16**, pp. 296–303, July 1978.
3. G. Franceschetti, M. Migliaccio, D. Riccio, and G. Schirinzi, "SARAS: A Synthetic Aperture Radar (SAR) Raw Signal Simulator," *IEEE Transactions on Geoscience and Remote Sensing* **30**, pp. 110–123, Jan. 1992.
4. R. K. Raney, "Synthetic Aperture Imaging Radar and Moving Targets," *IEEE Transactions on Aerospace and Electronic Systems* **7**, pp. 499–505, May 1971.
5. J. J. Sharma and M. J. Collins, "Simulation of SAR Signals from Moving Vehicles (Focusing Accelerating Ground Moving Targets)," *Proceedings of the 5th European Conference on Synthetic Aperture Radar EuSAR* **2**, pp. 841–844, May 2004.
6. S. R. J. Axelsson, "Position Correction of Moving Targets in SAR-Imagery," *Proceedings of SPIE* **5236**, pp. 80–92, Sept. 2003.
7. J. H. G. Ender, "Space-Time Processing for Multichannel Synthetic Aperture Radar," *Electronics and Communication Engineering Journal* **11**, pp. 29–38, Feb. 1999.
8. M. Soumekh, "Moving Target Detection and Imaging Using an X-Band Along-Track Monopulse SAR," *IEEE Transactions on Aerospace and Electronic Systems* **38**, pp. 315–333, Jan. 2002.
9. R. J. Sullivan, *Microwave Radar: Imaging and Advanced Concepts*, Artech House, Boston, 2000.
10. T. Sparr and B. Krane, "Oscillating Targets in Airborne SAR Images," *Proceedings of SPIE* **4883**, pp. 20–26, Mar. 2003.
11. T. Sparr and B. Krane, "Analysis of Phase Modulation Caused by Target Motion in SAR Images," *Proceedings of SPIE* **5102**, pp. 178–188, Apr. 2003.
12. T. Sparr and B. Krane, "Micro-Doppler Analysis of Vibrating Targets in SAR," *IEE Proceedings on Radar, Sonar and Navigation* **150**, pp. 277–283, Aug. 2003.
13. R. Bamler, "A Comparison of Range-Doppler and Wavenumber Domain SAR Focusing Algorithms," *IEEE Transactions on Geoscience and Remote Sensing* **30**, pp. 706–713, July 1992.
14. R. K. Raney, H. Runge, R. Bamler, I. G. Cumming, and F. H. Wong, "Precision SAR Processing Using Chirp Scaling," *IEEE Transactions on Geoscience and Remote Sensing* **32**, pp. 786–799, July 1994.
15. A. Moreira, J. Mittermayer, and R. Scheiber, "Extended Chirp Scaling Algorithm for Air- and Spaceborne SAR Data Processing in Stripmap and ScanSAR Imaging Modes," *IEEE Transactions on Geoscience and Remote Sensing* **34**, pp. 1123–1136, Sept. 1996.
16. D. Cerutti-Maori and U. Skupin, "First Experimental SCAN/MTI Results Achieved with the Multi-Channel SAR-System PAMIR," *Proceedings of the 5th European Conference on Synthetic Aperture Radar EuSAR* **2**, pp. 521–524, May 2004.
17. C. E. Livingstone, I. C. Sikaneta, C. H. Gierull, S. Chiu, A. Beaudoin, J. Campbell, J. Beaudoin, S. Gong, and T. A. Knight, "An Airborne Synthetic Aperture Radar (SAR) Experiment to Support RADARSAT-2 Ground Moving Target Indication (GMTI)," *Canadian Journal of Remote Sensing* **28**, pp. 794–813, Dec. 2002.
18. D. C. Schleher, *MTI and Pulsed Doppler Radar*, Artech House, Boston, 1991.